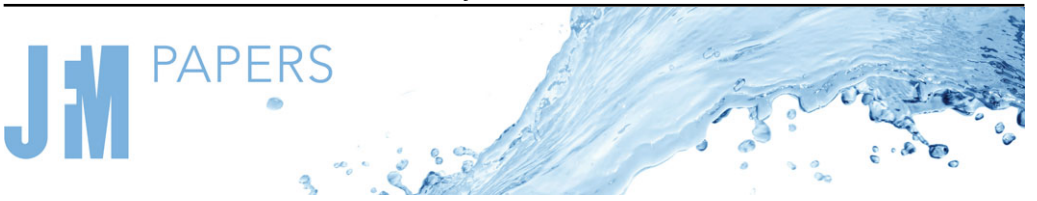
J. Fluid Mech. (2025), *vol.* 1011, A24, doi:10.1017/jfm.2025.396



Linear and nonlinear dynamics in radiatively forced cold water

Ruiqi Huang[1], **Zhen Ouyang**[1] **and Zijing Ding**[1,2]

[1]School of Energy Science and Engineering, Harbin Institute of Technology, Harbin, PR China

[2]Institute of Mechanics, Chinese Academy of Sciences, Beijing, PR China

Corresponding author: Zijing Ding, z.ding@hit.edu.cn

(Received 23 June 2024; revised 25 February 2025; accepted 8 April 2025)

This paper investigates the linear and nonlinear dynamics of two-dimensional penetrative convection subjected to radiative volumetric thermal forcing, focusing on ice-covered freshwater systems. Linear stability analysis reveals how critical wavenumbers k_c and Rayleigh numbers Ra_c are influenced by the attenuation lengths and incoming heat flux. In this configuration, the system easily becomes unstable with a small Ra_c, which is two decades smaller than that of the classical Rayleigh–Bénard convection problem, with typically $O(10)$. Weakly nonlinear analysis figures out that this configuration is supercritical, contrasting with the subcritical case by Veronis (*Astrophys. J.*, vol. 137, 1963, 641–663). Numerical bifurcation solutions are performed from the critical points and over several decades, up to $Ra \sim O(10^6)$. This paper found that the system exhibits multiple steady solutions, and under certain specific conditions, a staircase temperature profile emerges. Meanwhile, we further discuss the influence of incoming heat flux and the Prandtl number Pr on the primary bifurcation. Direct numerical simulations are also carried out, showing that heat is transported more efficiently via unsteady convection.

Key words: buoyancy-driven instability, bifurcation

1. Introduction

Thermal convection is a common phenomenon that occurs in many natural and industrial systems. The thermal convection inside the mantle is driven by radioactive decay (Davaille & Jaupart 1994; Ricard 2007; Schubert 2015), and in industrial cases, fluids may be internally heated or cooled by chemical reactions (Ponce *et al.* 2015; Shen & Zikanov 2016). These phenomena are often modelled by the classical Rayleigh–Bénard convection (RBC) (Bergé & Dubois 1984; Bodenschatz *et al.* 2000; Grossmann & Lohse 2004; Plumley & Julien 2019), which provides a foundational framework for understanding buoyancy-driven flows between heated and cooled boundaries. However, natural and

© The Author(s), 2025. Published by Cambridge University Press.

https://doi.org/10.1017/jfm.2025.396 Published online by Cambridge University Press

industrial systems often exhibit complexities – such as internal heating, phase changes and radiative forcing – that extend beyond the classical RBC framework (Kippenhahn & Weigert 1990; Barker *et al.* 2014; Hussein *et al.* 2014; Ponce *et al.* 2015; Shen & Zikanov 2016; Álvarez-Regueiro *et al.* 2019).

Penetrative convection occurs when buoyancy-driven flows invade stably stratified regions, a process ubiquitous in astrophysical, oceanic and limnological systems (Ding *et al.* 2024). A key factor governing this process is the presence of a uniform internal heating source, which produces a quadratic conductive temperature profile and significantly alters the stability and dynamics of the system (Goluskin & Spiegel 2012; Goluskin 2016; Goluskin & van der Poel 2016). Additionally, the nonlinear relationship between fluid density and temperature plays a critical role in driving penetrative convection (Veronis 1963; Musman 1968; Lecoanet *et al.* 2015; Toppaladoddi & Wettlaufer 2018; Ding & Wu 2021; Olsthoorn *et al.* 2021; Grace *et al.* 2022; Ding & Ouyang 2023). For example, freshwater exhibits special properties, especially its maximum density at approximately 4 °C, which usually conforms to a quadratic constitutive relation:

$$\rho = \rho_0(1 - \alpha(T - T_M)^2), \tag{1.1}$$

where $\alpha > 0$ is the thermal expansion coefficient and ρ_0 is the density at $T = T_M$. Chen & Millero (1986) proposed this quadratic relationship to approximate the full equation of state and McDougall *et al.* (2003) extensively researched and demonstrated that freshwater between 0 and 10 °C satisfies this relationship. Although the choice of the exponent has an impact on the accuracy of the model (Gebhart & Mollendorf 1977; Wang *et al.* 2019), this simple and concise quadratic formula, derived from the Taylor series, helps maintain significant nonlinearity. The typical ice–water model was proposed by Malkus (1960) and analysed by Veronis (1963). Veronis (1963) explored the linear stability of the ice–water model heated from below between two stress-free walls. The author discovered that the instability is suppressed by increasing the thickness of the stably stratified layer and it reduces heat transfer efficiency by causing multiple convection cells to form in the wall-normal direction. Subsequent studies demonstrated that penetrative convection can exhibit subcritical instability, where finite-amplitude disturbances destabilise flows below the linear critical Rayleigh number Ra_c (Musman 1968; Moore & Weiss 1973; Joseph 1976). A series of further analyses, such as finding the rigorous upper bound, weakly nonlinear analysis (Veronis 1963; Ding & Wu 2021; Olsthoorn *et al.* 2021), were based on this model and laid a theoretical foundation for the research in this field.

Recent advances in limnology and environmental fluid dynamics have highlighted the hydrodynamic complexity of ice-covered lakes, where solar absorption drives convective mixing and stratification (Farmer 1975; Bengtsson 1996; Mironov *et al.* 2002; Toppaladoddi & Wettlaufer 2018; Ulloa *et al.* 2018). Compared with ice-free periods, the conditions inside ice-covered lakes are more complicated due to solar radiation and the properties of water, which were initially studied during the early 1900s (Gotzinger 1909; Verescagin 1925). In the presence of solar radiation, water undergoes stratification in density, resulting in the coexistence of an unstably stratified region and a stably stratified layer. Matthews & Heaney (1987) demonstrated that hydrodynamic processes in lakes become more energetic and dynamic when increased solar radiation penetrates into the system in late winter or spring. Farmer (1975) and Mironov *et al.* (2002) further shaped the flow patterns and the modifications to vertical and horizontal convective circulation. Several reviews have summarised the current research status of seasonally ice-covered lakes (Kirillin *et al.* 2012; Powers & Hampton 2016; Jansen *et al.* 2021). Powers & Hampton (2016) focused on the ecosystem dynamics of ice-covered lakes. Jansen *et al.* (2021) provided an overview of the physical processes in ice-covered lakes and highlighted

https://doi.org/10.1017/jfm.2025.396 Published online by Cambridge University Press

the hydrodynamic problems involved, including the physical basis of lake ice phenology and the heat transfer mechanisms associated with ice formation and melting. They also pointed out that when energy enters the system, understanding and predicting the temporal and spatial variability of water layers are the key to solving these problems.

Over the past decade, convection processes within ice-covered lakes, which are normally called radiatively driven convection (RDC), have been investigated theoretically (Matthews & Heaney 1987; Kirillin & Terzhevik 2011; Winters *et al.* 2019), numerically (Bouffard *et al.* 2019; Ulloa *et al.* 2019; Ramón *et al.* 2021; Christopher *et al.* 2023) and experimentally (Efremova & Pal'shin 2011; Yang *et al.* 2017, 2020; Cortés & MacIntyre 2020). For example, Efremova & Pal'shin (2011) conducted research on water bodies in northwestern Russia to explore the link between air temperature, geographical features and ice phenomena. They found that the depth of individual lakes plays a more significant role in the freeze-up process than climatic factors. Bouillaut *et al.* (2019) and Lepot *et al.* (2018) performed laboratory experiments to investigate RDC by means of light absorption. With the linear relationship $\rho = \rho_0(1 - \alpha(T - T_0))$ and an exponential internal heating source, Lepot *et al.* (2018) conducted direct numerical simulations (DNS) and found that specific equilibrium profiles of internal heat sources and sinks may facilitate heat transfer at a rate transcendent of molecular diffusivities.

From observation studies, a time-dependent radiation model was proposed to account for periodic heating (Leppäranta *et al.* 2010; Zdorovennova *et al.* 2021) and attracted the attention of the community of environmental science and limnology recently (Smirnov *et al.* 2022; Chang & Scotti 2023; Smirnov *et al.* 2023). This kind of convection also plays a significant role in ice melting and freezing (Wang *et al.* 2021; McCutchan & Johnson 2022). For scenarios with floating ice, a series of ice-melting researches have set the ice–water interface at 0 °C. Wang *et al.* (2021) provided good insight into how RDC affects ice melting and freezing. They also modelled and examined this system theoretically, numerically and experimentally and provided a good insight into the hydrodynamic process beneath the ice. They also showed that the behaviour of the density surrounding the temperature of maximum density results in stably or unstably stratified layers, which is also detected in laboratory experiments (McCutchan & Johnson 2022). To deeply study this kind of convective system, it is crucial to investigate the impact of nonlinear fluid properties. Wang *et al.* (2019) studied how this nonlinear temperature–density relationship and uniform internal heat source changed convection processes and analysed their impacts on heat transport and flow strength.

To understand how the underwater hydrodynamics influences the ecology of ice-covered lakes during seasonal ice-covered periods (Hampton *et al.* 2017), it is important to investigate the vertical heat transfer processes involving water flow within ice-covered lakes located at mid to high latitudes and high altitudes. This aspect has been inadequately studied in the past. Although the dynamics of radiatively heated ice-covered lakes has been extensively studied, prior research has predominantly focused on turbulent flows (Ulloa *et al.* 2019; Smirnov *et al.* 2023). Critical questions regarding the extent to which solar radiation drives under-ice convection and the role of light distribution in triggering its onset remain unresolved. This study addresses these gaps through integrated linear stability analysis, weakly nonlinear theory and DNS, focusing on the stability and bifurcation dynamics of radiatively heated ice-covered freshwater systems. Furthermore, the investigation incorporates weakly and fully nonlinear analyses to provide a theoretical and numerical assessment of how solar radiation influences vertical heat transfer and dynamic behaviour.

The structure of the paper is organised as follows. Section 2 mathematically formulates the problem and § 3 shows the base state and examines the linear stability of this

https://doi.org/10.1017/jfm.2025.396 Published online by Cambridge University Press

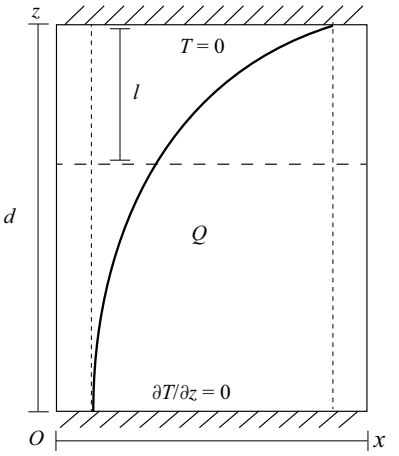


Figure 1. Internally heated convection model with an internal heating source Q, as expressed in equation (2.1). The decay scale of Q is l, and the e-folding scale is located at a height $d - l$. The model has an isothermal top layer and an insulating bottom layer.

system. To describe and understand the instability of the system, weakly nonlinear analysis is applied in § 4 to help us identify the type of primary bifurcation. Fully nonlinear bifurcation and DNS are shown in § 5. A summary and discussion are provided in § 6.

2. Mathematical formulation

This study considers a Newtonian fluid under the Boussinesq approximation, with density ρ, kinematic viscosity ν and thermal diffusivity κ. The fluid is bounded between two horizontal no-slip plates with a gap of width d, where the top plate is usually considered as an ice–water interface and the bottom is perfectly insulating. By considering a monochromatic light spectrum, the system has an internal heat source $Q(z)$ ($^{\circ}\mathrm{C\,s^{-1}}$), as sketched in figure 1. It is a simplified model of a short-wave radiation that is characterised by a single decay scale (Bouillaut *et al.* 2019; Creyssels 2020). According to the Beer–Lambert law, this type of heating is associated with a volumetric heat source that decays exponentially (Barnes & Hobbie 1960; Farmer 1975; Grace *et al.* 2022, 2023):

$$Q(z) = \frac{Q_0}{l} \exp\left(\frac{z-d}{l}\right), \tag{2.1}$$

where l is the attenuation length, which normally depends on radiation frequency and water clarity, and Q_0 is the magnitude of the thermal forcing at the top of the domain. Polychromatic light has a different effect: the heat flux is the sum of different wavelength bands that have different energy and attenuation depths (Mironov *et al.* 2002; Bouffard *et al.* 2019; Smirnov *et al.* 2023).

Two additional models were also employed to investigate convection in lakes. When light penetrates the water column and reflects off the bottom, a reverse exponential decay happens from the bottom to the top. The intensity of the reflected light $I(z)$ at a depth z (measured from the surface) can be modelled as similar to equation (2.1) but with a bottom heat flux Q_{bottom}. This model can well represent shallow aquatic systems or environments where the bottom strongly reflects light (sandy or icy bottoms) (Lepot *et al.* 2018; Bouillaut *et al.* 2019). If we consider that the bottom of the lake can absorb heat and re-inject it into the fluid, then we can regard it as a simple penetrative convection problem of bottom

https://doi.org/10.1017/jfm.2025.396 Published online by Cambridge University Press

heating. In this case, there is a constant temperature difference between the upper and lower boundaries of the convection system (Veronis 1963).

The dimensionless governing equations can be obtained by introducing the layer height d as the length scale and d^2/κ as the thermal time scale. The temperature scale is $\Delta T = T_M - T_0$, where $T_0 = 0\,^\circ\mathrm{C}$ is the reference temperature and $T_M = 4\,^\circ\mathrm{C}$. Thus $\theta = (T - T_0)/\Delta T$ is the dimensionless temperature and $\theta_M = (T_M - T_0)/\Delta T$ describes the effect under the maximal density with $\theta_M = 1$. Then the dimensionless governing equations for two-dimensional penetrative convection are as follows:

$$\nabla \cdot \boldsymbol{u} = 0, \tag{2.2}$$

$$\frac{\partial \boldsymbol{u}}{\partial t} + \boldsymbol{u} \cdot \nabla \boldsymbol{u} = -\nabla p + Pr\,Ra(\theta - 1)^2 \boldsymbol{e}_z + Pr\nabla^2 \boldsymbol{u}, \tag{2.3}$$

$$\frac{\partial \theta}{\partial t} + \boldsymbol{u} \cdot \nabla \theta = \nabla^2 \theta + S(z), \tag{2.4}$$

where $Ra := g\alpha(\Delta T)^2 d^3/\nu\kappa$ is the Rayleigh number and $Pr := \nu/\kappa$ is the Prandtl number, and

$$S(z) = \frac{M}{\delta} \exp\left(\frac{z-1}{\delta}\right). \tag{2.5}$$

Here, $\delta := l/d$ and $M := dQ_0/(\Delta T\kappa)$ are dimensionless parameters that quantify attenuation length and incoming thermal forcing, respectively. Once radiation penetrates through the ice, the value of Q_0 is about $7.25 \times 10^{-6}\,^\circ\mathrm{C}\cdot\mathrm{m\,s^{-1}}$ (Kirillin *et al.* 2012; Ulloa *et al.* 2019; Grace *et al.* 2022). Assuming that $d = 1$ m and taking freshwater as an example ($\kappa = 10^{-7}\,\mathrm{m^2\,s^{-1}}$), we estimate $M = 18.125$. We chose the range of δ from 0.1 to 0.8 to examine the impacts of both smaller and larger attenuation lengths. By integrating the heat flux $S(z)$, the total heat input to the system is

$$E = \int_0^1 \frac{M}{\delta} \exp\left(\frac{z-1}{\delta}\right) \mathrm{d}z = M\left(1 - \exp\left(-\frac{1}{\delta}\right)\right). \tag{2.6}$$

Clearly, the total energy input increases when M is larger. For given M, the total energy input decreases as δ increases.

The boundary conditions for velocity and temperature are

$$\boldsymbol{u}|_{z=0,1} = 0, \tag{2.7}$$

$$\partial_z \theta|_{z=0} = 0, \quad \theta|_{z=1} = 0. \tag{2.8}$$

To investigate the heat transport efficiency of the system, we start from the definition of heat flux:

$$q := \frac{\lambda(T_{bottom} - T_{top})}{d}, \tag{2.9}$$

where λ is the thermal conductivity. Applying the boundary conditions, we have a fixed temperature at the top layer, $T_{top} = 0\,^\circ\mathrm{C}$. In our configuration, the Nusselt number is defined as q_{cond}/q_{conv} (q_{cond} and q_{conv} are the conductive and convective heat fluxes, respectively) to reflect the influence of the intensity of convection on the heat transport, and calculated as (Goluskin 2016; Kazemi *et al.* 2022)

$$Nu = \frac{\theta_{st}(0)}{\bar{\theta}(0)}, \tag{2.10}$$

https://doi.org/10.1017/jfm.2025.396 Published online by Cambridge University Press

where θ_{st} is the dimensionless base state solution to the temperature equation with $\boldsymbol{u} = \boldsymbol{0}$. The detailed expression can be found in equation (3.2). The overbar denotes an average over the horizontal surfaces and long enough time with

$$\bar{(\cdot)} = \frac{1}{\tau L}\int_0^\tau \mathrm{d}t \int_0^L (\cdot)\,\mathrm{d}x, \tag{2.11}$$

where τ can be arbitrary for steady solutions, and for turbulent flows it is chosen as four thermal times in simulations when the flow is fully developed.

3. Base state and instability

Firstly, we consider a static base state:

$$\boldsymbol{u} = \boldsymbol{0}, \quad \frac{\partial^2 \theta_{st}}{\partial z^2} + S(z) = 0. \tag{3.1}$$

Thus, static state temperature θ_{st} is

$$\begin{gathered}\theta_{st} = -M\delta \exp\left(\frac{z-1}{\delta}\right) + C_1 z + C_2, \\ C_1 := M \exp\left(-\frac{1}{\delta}\right), \quad C_2 := M\delta - M\exp\left(-\frac{1}{\delta}\right).\end{gathered} \tag{3.2}$$

The water body beneath the ice is heated via radiation which is the only form of energy input of the system. Figure 2(*a*) represents the base state of the temperature for varied attenuation depths and the corresponding density profiles are displayed in figure 2(*b*). As the density is quadratically dependent on temperature, the water body is stratified into a stably stratified layer (SSL), whose temperature ranges from 0 to θ_M, and an unstably stratified layer (USL). When most radiation is absorbed near the ice–water interface, characterised by a small attenuation depth δ, fluid deep in the water body cannot be efficiently heated and maintains a uniform temperature, forming a neutrally stratified layer (NSL). For a system with larger δ, the depth of the NSL becomes smaller and the USL is thicker. However, when radiation penetrates even deeper, the magnitude of radiation absorbed by the water body, characterised by M/δ, is lower. Therefore, the system reaches a maximum bottom temperature $\theta_{st}(0) \approx 5.40$ and a minimum density $\rho_{st}(0)$ at $\delta \approx 0.56$ when $\mathrm{d}\theta_{st}(0)/\mathrm{d}\delta = 0$.

We add small perturbations to the base state, and then the velocity field and temperature field become

$$\boldsymbol{u} = \boldsymbol{0} + \tilde{\boldsymbol{u}}, \quad \theta = \theta_{st} + \tilde{\theta}. \tag{3.3}$$

For two-dimensional incompressible flow, we can introduce a streamfunction ψ defined as $\tilde{\boldsymbol{u}} = \nabla \times (\psi \boldsymbol{e}_y)$ such that

$$\tilde{u} = -\partial_z \psi, \quad \tilde{w} = \partial_x \psi. \tag{3.4}$$

Therefore, the linearised equations for small perturbations are given by

$$\frac{\partial}{\partial t}(\nabla^2 \psi) = 2PrRa(\theta_{st} - 1)\frac{\partial \tilde{\theta}}{\partial x} + Pr\nabla^2(\nabla^2 \psi), \tag{3.5}$$

$$\frac{\partial \tilde{\theta}}{\partial t} + \frac{\partial \psi}{\partial x}\frac{\partial \theta_{st}}{\partial z} = \nabla^2 \tilde{\theta}, \tag{3.6}$$

https://doi.org/10.1017/jfm.2025.396 Published online by Cambridge University Press

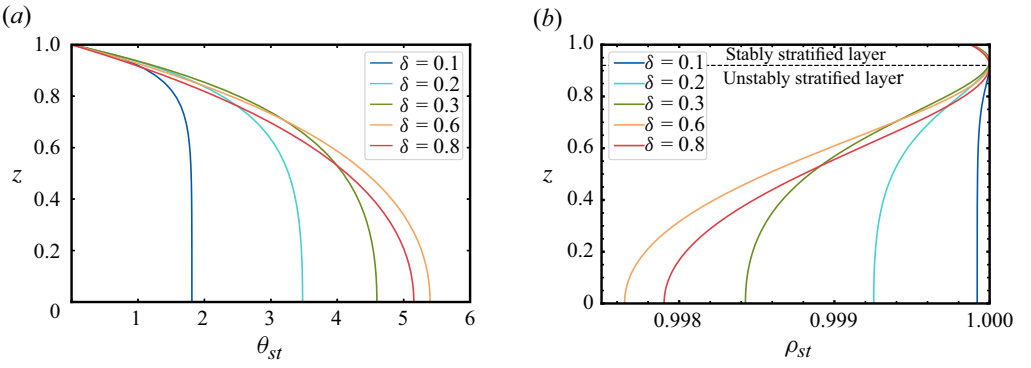


Figure 2. (*a*) The static state temperature profiles θ_{st} with respect to the height z for varied attenuation ratios δ. (*b*) The corresponding static state density profiles ρ_{st} for different δ. The horizontal dashed line is the dividing line between the SSL and the USL.

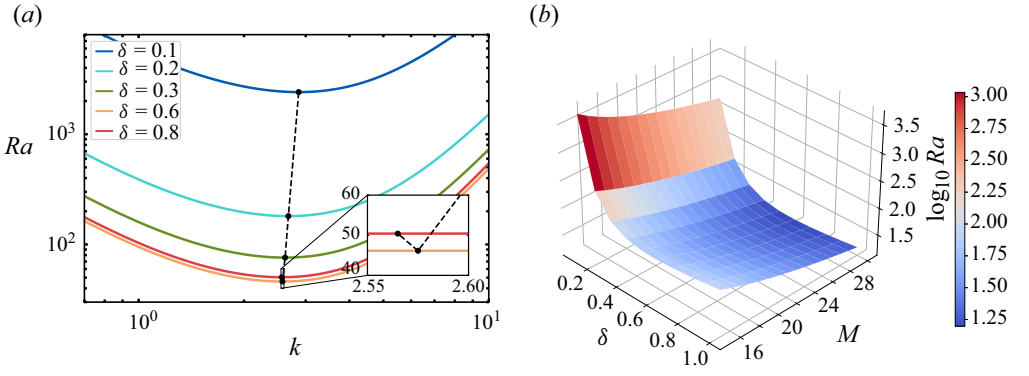


Figure 3. (*a*) Marginal stability curve in the wavenumber (k)–Rayleigh number (Ra) plane under different attenuation ratios δ from 0.1 to 0.8, with a fixed thermal forcing $M = 18.1250$. (*b*) The surface plot shows how the critical Rayleigh number Ra_c is affected by M and δ, for $15 \leqslant M \leqslant 30$ and $0.1 \leqslant \delta \leqslant 1$.

and the corresponding boundary conditions become

$$\psi|_{z=0,1} = \partial_z \psi|_{z=0,1} = 0,$$
$$\partial_z \tilde{\theta}|_{z=0} = 0, \quad \tilde{\theta}|_{z=1} = 0. \tag{3.7}$$

In a standard way, we conduct the normal mode analysis:

$$\tilde{\psi} = \hat{\psi}(z) e^{ikx+\sigma t}, \quad \tilde{\theta} = \hat{\theta}(z) e^{ikx+\sigma t}, \tag{3.8}$$

where k is the wavenumber and σ is the growth rate. Then the governing equation is transformed into an eigenvalue problem of σ.

The relationship between the critical Rayleigh numbers Ra_c and wavenumbers k is shown in figure 3(*a*). The dashed line directly indicates that the relationship between Ra_c and critical wavenumber k_c is not monotonic. Within our tested range, Ra_c has a minimum point around $\delta = 0.6$ (as shown in the inset) with $Ra_c \sim O(10)$, which is two decades smaller than that in classical RBC: $Ra_c \sim O(10^3)$ (Chandrasekhar 1961; Cross & Hohenberg 1993). Intuitively, we expect to observe a more stable flow if the input energy is reduced. However, when δ increases up to 0.6, the thickness of the USL increases even though the energy input decreases. Thus, the system can be more unstable and the critical

https://doi.org/10.1017/jfm.2025.396 Published online by Cambridge University Press

Rayleigh number becomes smaller. As δ becomes larger ($\delta > 0.6$), further reduction in the input energy causes a thinner unstable layer, leading to a more stable system. Thus, we observe that the critical Rayleigh number increases when $\delta > 0.6$. Furthermore, we took a transect through the plane presented in figure 3(*b*). Results are shown in figure 16 in Appendix A. It is clear that the system would be more unstable as the total input energy becomes higher.

The surface plot presented in figure 3(*b*) provides a detailed view of how Ra_c is influenced by the two dimensionless parameters δ and M. We chose the ranges of $15 \leqslant M \leqslant 30$ and $0.1 \leqslant \delta \leqslant 1$ to examine the influence of incoming heat thermal heat flux and forcing length scales on the linear and nonlinear dynamics. If the attenuation depth is fixed, an increase in the incoming heat flux (M) would lead to a higher temperature difference within the USL. This suggests that the system retains more heat, resulting in a lower density in the unstable stratified layer, eventually leading to a lower Ra_c and making the system unstable easily.

4. Weakly nonlinear stability

To analyse the convective flow, it is crucial to incorporate the nonlinear terms into the system. Therefore, we conduct a weakly nonlinear analysis of the system, focusing on the dynamics near Ra_c. We aim to identify the specific type of local bifurcation it undergoes. To investigate weakly nonlinear solutions, we use multi-scale expansion and determine solvability conditions.

The governing equations (2.3)–(2.4) are restated by the streamfunction and temperature:

$$\frac{\partial \nabla^2 \psi}{\partial t} + J(\psi, \nabla^2 \psi) = 2RaPr(\theta_{st} - 1 + \tilde{\theta})\frac{\partial \tilde{\theta}}{\partial x} + Pr\nabla^4 \psi, \tag{4.1}$$

$$\frac{\partial \tilde{\theta}}{\partial t} + J(\psi, \tilde{\theta}) = -\frac{\partial \psi}{\partial x}\frac{\partial \theta_{st}}{\partial z} + \nabla^2 \tilde{\theta}, \tag{4.2}$$

where $J(\alpha, \beta) = (\partial\alpha/\partial x)(\partial\beta/\partial z) - (\partial\alpha/\partial z)(\partial\beta/\partial x)$ and the boundary conditions are with reference to equation (3.7).

When Ra is slightly larger than Ra_c, there is an unstable mode that becomes dominant through linear theory, whereas other modes decay exponentially in time. However, the unstable mode in linear theory cannot reveal the full dynamics of the problem as the nonlinear term would be significant when the perturbation grows. We invoke the multi-scale analysis and define a small parameter ϵ:

$$\epsilon^2 r = Ra - Ra_c, \quad |Ra - Ra_c| \ll 1, \tag{4.3}$$

where r is a rescaled parameter of $r \sim O(1)$ and the slow time scale τ is defined as

$$\tau = \epsilon^2 t. \tag{4.4}$$

Thus, this leads us to the assumption that the weakly nonlinear solution is of the form

$$\psi(x, z, \tau) := \epsilon^{\alpha}\hat{\psi}_1(z)\mathrm{e}^{ikx}A(\tau) + \epsilon^{2\alpha}\left[\hat{\psi}_{20}(z) + \hat{\psi}_{22}(z)\mathrm{e}^{i2kx}\right]A^2(\tau) + \cdots + \text{c.c.} \tag{4.5}$$

$$\tilde{\theta}(x, z, \tau) := \epsilon^{\alpha}\hat{\theta}_1(z)\mathrm{e}^{ikx}A(\tau) + \epsilon^{2\alpha}\left[\hat{\theta}_{20}(z) + \hat{\theta}_{22}(z)\mathrm{e}^{i2kx}\right]A^2(\tau) + \cdots + \text{c.c.} \tag{4.6}$$

https://doi.org/10.1017/jfm.2025.396 Published online by Cambridge University Press

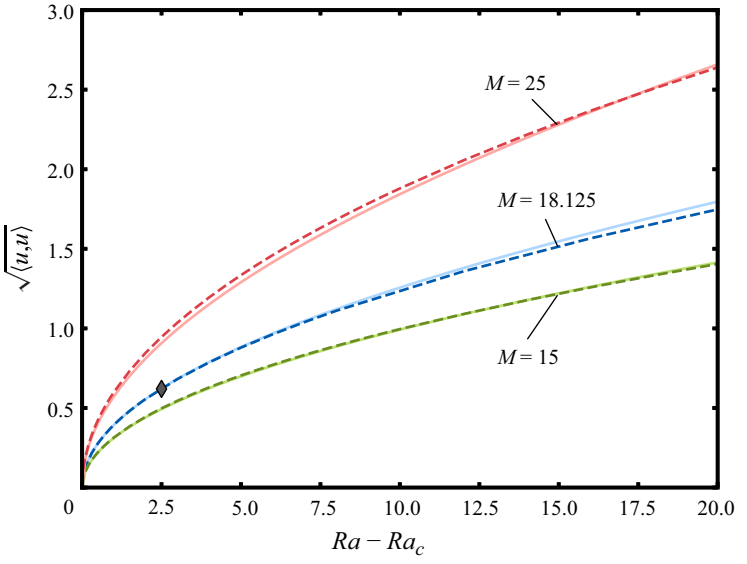


Figure 4. Comparison of the weakly nonlinear analysis with a full branch continuation prediction at the neighbourhood of the critical Rayleigh number Ra_c for $\delta = 0.6$ and different M. Values of $\sqrt{\langle \boldsymbol{u}, \boldsymbol{u} \rangle}$ are taken over the whole domain $\Omega = [-\pi/k, \pi/k] \times [0, 1]$ with equation (B24) defined in Appendix B. The dashed lines are the results from full branch continuation and the solid lines are for weakly nonlinear analysis.

The system of equations possesses a unique set of solutions if and only if it satisfies a solvability condition, which yields the following Landau-type equation:

$$\frac{\mathrm{d}A}{\mathrm{d}\tau} = \lambda_1 r A + \lambda_2 |A|^2 A, \tag{4.7}$$

where λ_1 and λ_2 are constants (see Appendix B). The Landau equation (4.7) defines the amplitude function and is used to determine whether the stability is supercritical or subcritical. The equilibrium amplitude can be solved as

$$A_{eq} = \sqrt{-\frac{\mathrm{Re}(\lambda_1) r}{\mathrm{Re}(\lambda_2)}}. \tag{4.8}$$

Notice that the supercriticality or the subcriticality of the bifurcation depends on the sign of $\mathrm{Re}(\lambda_1)$ and $\mathrm{Re}(\lambda_2)$. If $\mathrm{Re}(\lambda_1) \cdot \mathrm{Re}(\lambda_2) < 0$, the system will reach the stable steady solutions when $r > 0$. On the contrary, if they have the same sign, non-trivial solutions exist when r is negative in the system for $Ra < Ra_c$ and is normally known as a subcritical bifurcation (Schmid & Henningson 2002). By examining different factors, we determined that the instability of this configuration is always supercritical for all δ and M considered. As shown for results obtained with weakly nonlinear analysis (figure 4), there is a bifurcation branch at $\sqrt{\langle \boldsymbol{u}, \boldsymbol{u} \rangle} = 0$ that is stable for $Ra < Ra_c$ and unstable for $Ra > Ra_c$. At Ra_c, a stable branch of solutions emerges. This means that the finite-amplitude equilibrium state would be achieved if the static state loses stability. An obvious finding is that with an increase of M, the greater the temperature difference in the USL, the stronger the buoyancy, and therefore the greater the kinetic energy.

Compared to the Veronis model (Veronis 1963), the involvement of the internal heating source and a perfect insulating bottom layer in our model leads to different interesting dynamics. The Veronis model argued that with a finite-amplitude perturbation, the mixing would increase the thickness of the unstably stratified layer (Moore & Weiss 1973),

https://doi.org/10.1017/jfm.2025.396 Published online by Cambridge University Press

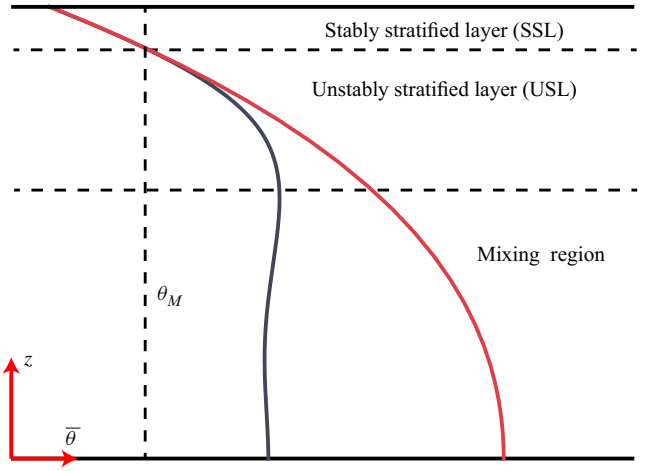


Figure 5. Schematic diagram of mean temperature profiles $\bar{\theta}$ of base state and convection. The red line represents the base state and the black line convection. The vertical dashed line gives the position of $\theta = \theta_M$.

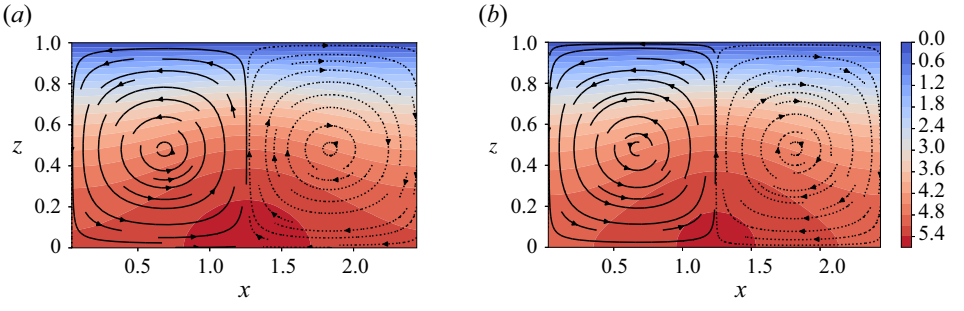


Figure 6. The flow field and temperature field predicted by full branch continuation (a) and weakly nonlinear analysis (b) techniques at point $\diamond$. The colour bar marks the contours of the temperature field.

resulting in loss of instability at smaller $Ra < Ra_c$. Such convection is sustainable via the nonlinear mechanism. Yet in our model, the nonlinear mechanism forms a homogeneous layer near the bottom. In this case, the USL becomes thinner (as shown in figure 5) and thus enhances stability. Therefore, convection always appears via a supercritical pitchfork bifurcation.

By comparing the results obtained from the weakly nonlinear analysis with those derived from a fully nonlinear branch, the weakly nonlinear solutions are in agreement with the fully nonlinear solution in the neighbourhood of critical states and start to diverge for higher Rayleigh numbers away from the critical point (see figure 4). Such divergence is originated from the truncation error in weakly nonlinear methods, which would be larger for stronger convection intensity, i.e. larger $||u||_E$, induced from more intense radiation, i.e. larger M. Naturally, this divergence results from the weakly nonlinear analysis using a three-mode expansion as opposed to the full branch continuation curve which uses 60 Fourier modes. This low-order approximation serves as a valuable method for comparing the behaviour of the system under various conditions in the neighbourhood of critical points. Figure 6 presents a comparison between steady solutions derived from the two methods, showing both flow fields and temperature fields at the specific point $\diamond$ (marked

https://doi.org/10.1017/jfm.2025.396 Published online by Cambridge University Press

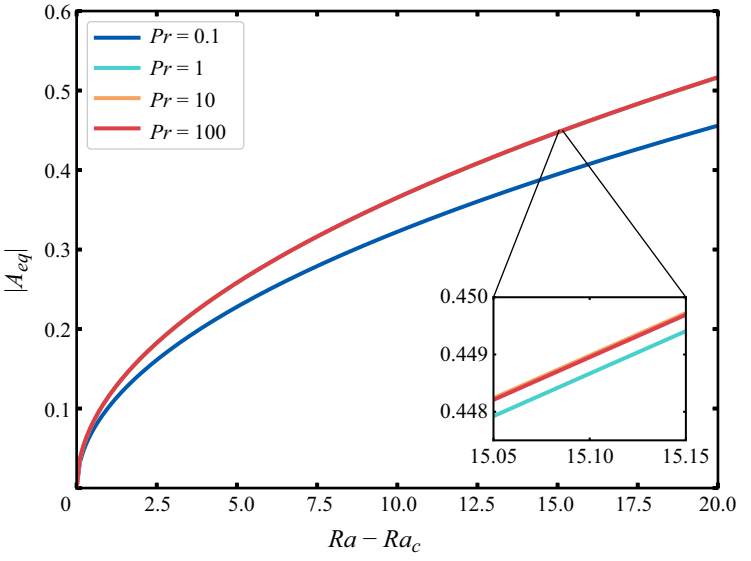


Figure 7. Variation of equilibrium amplitude $|A_{eq}|$ as a function of Rayleigh number for different values of Pr at $\delta = 0.3$.

in figure 4). It has been observed that there is one pair of convective cells exhibiting highly similar convection patterns.

Furthermore, our model can be extended to other materials. For example, the density of tellurium–cadmium–mercury alloys ($Pr \approx 0.1-0.5 < 1$) also quadratically depends on temperature, similar to water. Thus, we considered a wide range of Pr to study its influence on the nonlinear solutions. However, most of our results are for $Pr = 10$, i.e. for freshwater. We also determined that the bifurcation behaviours are supercritical for different Prandtl numbers. Figure 7 illustrates the equilibrium amplitude (A_{eq}) away from the critical point. With higher Pr, the magnitude of $|A_{eq}|$ increases. We assume that when the thermal diffusivity remains constant, a higher Pr corresponds to a more viscous fluid. Thus, it means that the system needs more energy to drive fluid motion and results in a larger equilibrium amplitude $|A_{eq}|$. The observation that $|A_{eq}|$ becomes invariant for $Pr > 10$ indicates that beyond a certain threshold, further increases in Pr do not significantly affect the equilibrium amplitude. This indicates that the influence of the Prandtl number diminishes, as inertial effects become negligible when Pr is large.

5. Fully nonlinear dynamics

When $Ra > Ra_c$, the flow becomes unstable and convection cells will form. We seek steady convection cell solutions using the Newton method and a pseudo-arclength continuation technique to track the branches. The details of this method can be found in Appendix C. To obtain non-trivial steady solutions, we added the critical mode to the base state as the initial guess of the Newton iteration. Moving slightly away from the critical point indicated by the linear stability, convergence happens quickly when the amplitude of the eigenvector is well chosen. The amplitude can be chosen from the weakly nonlinear analysis. We also used DNS and simulated 10 thermal times to understand the behaviour of the system, and the snapshots are taken at $t_{thermal} = 10\,\mathrm{s}$. A Fourier-spectral method was employed to discretise the spatial domain and a finite-difference method was used with non-uniform grids that cluster near the walls (Chebyshev points).

https://doi.org/10.1017/jfm.2025.396 Published online by Cambridge University Press

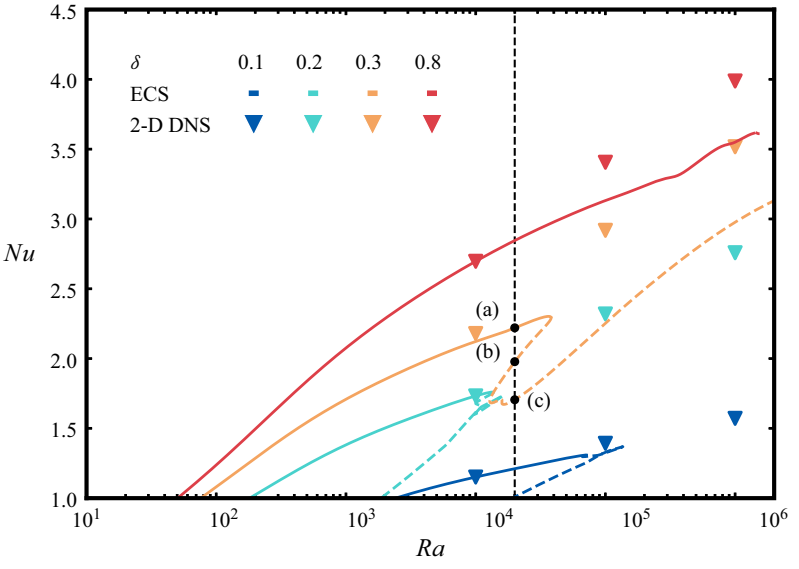


Figure 8. The bifurcation diagram in the Ra–Nu plane representing exact coherent solutions (ECS) and two-dimensional DNS results for different attenuation depths δ. The Prandtl number $Pr = 10$ and the dimensionless heat flux $M = 18.125$. The vertical dashed line indicates the location of $Ra = 2 \times 10^4$.

The time discretisation was accomplished with a second-order Adams–Bashforth–Crank–Nicolson method. The numerical method is adapted based on Ding & Wu (2021) and Ding & Ouyang (2023).

The bifurcation diagram is plotted in the $Ra-Nu$ plane for varied values of δ. We chose the fixed domain width $[-\pi/k_c, \pi/k_c]$, where k_c is the critical wavenumber of instability. Near the critical bifurcation points, figure 8 aligned with the results gained from the weakly nonlinear analysis that the instability is supercritical for all δ. The bifurcation of the system is calculated up to $Ra \sim O(10^6)$, alongside two-dimensional DNS results, where the average Nusselt number is obtained after convection is fully developed. When $\delta = 0.8$, figure 9(a) shows the mean temperature profiles $\bar{\theta}$ for two-dimensional exact coherent states for $Pr = 10$ and different Ra. As Ra increases and convection strengthens, the dimensionless temperature decreases, and the interior of the system strongly mixes and becomes closer to isothermal. When convection is sufficiently strong, the maximum value of $\bar{\theta}$ shifts from the bottom boundary to a location inside the layer. Figure 9(b,c) illustrates the flow fields and the temperature fields of the steady solution and unsteady motions for $Ra = 10^6$. The DNS results in figure 9(c) show that the unsteady motions cause the fluid to mix strongly and become closer to isothermal. The temperature becomes uniform within the mixing region. Plumes arise from the USL upper boundary layer and vigorously blend the fluid in the remaining area. Together with the numerical results shown in figure 8, the Nusselt number of the unsteady motion (figure 9c) is $Nu \approx 4$, whereas the steady solution (figure 9b) has $Nu \approx 3.5$. Thus, the unsteady motion transports heat more efficiently.

Returning to figure 8, it is obvious that the system would experience a saddle-node bifurcation when δ is small and the dashed lines indicate that they are unstable. An interesting observation is that there are multiple steady solutions for the same Rayleigh number. Taking $\delta = 0.3$ for example, there are three steady solutions at $Ra = 20\,000$ and figure 10(a–c) illustrates the flow fields and temperature fields for each solution. There is a pair of same-sized convection cells in the system at point (a); however, at points (b) and (c), the shape of convection cells gradually changed and several small-sized convection

https://doi.org/10.1017/jfm.2025.396 Published online by Cambridge University Press

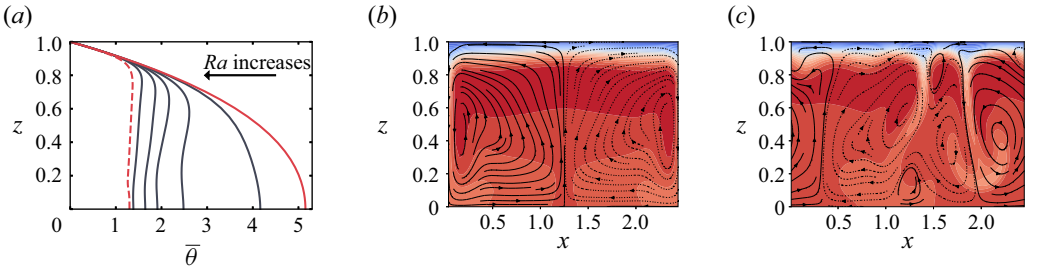


Figure 9. (*a*) The mean temperature field $\bar{\theta}$ for $\delta = 0.8$. The red solid line is that of the base state and the red dashed line is that of DNS at $Ra = 10^6$. The others, from right to left, are from the steady-state solutions for $Ra = (0.01, 0.1, 1, 10, 100) \times 10^4$. Flow fields and temperature fields from (*b*) two-dimensional steady solution and (*c*) DNS at $Ra = 10^6$.

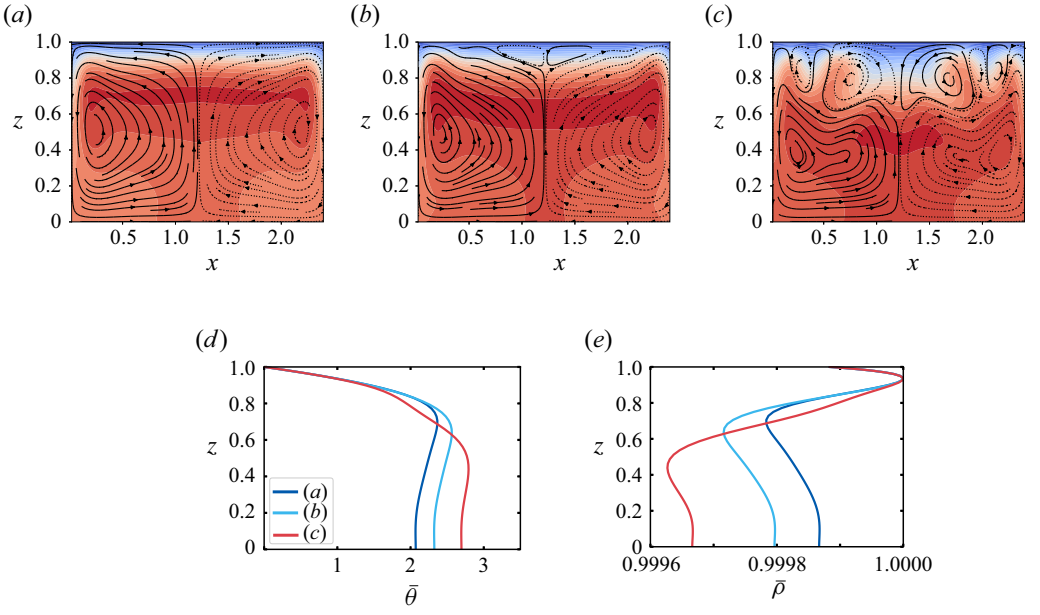


Figure 10. The flow field and temperature field at $Ra = 20\,000$ and $Pr = 10$, $\delta = 0.3$. (*a*) The upper branch solution, (*b*) the middle branch solution and (*c*) the lower branch solution. (*d*) The horizontal mean temperature profile $\bar{\theta}$ for the three cases. (*e*) The corresponding density profiles for the three cases.

cells appeared, which impeded the effective heat transport with smaller Nu. Our results suggest that the form of a pair of convection cells does not exist if Ra exceeds a certain value, and a saddle-node bifurcation takes place and connects to the bifurcation branch of the solutions with multiple pairs of convection cells. By analysing the corresponding mean temperature and density profiles (as shown in figure 10*d*,*e*), we determined that at case (*c*), the USL becomes thicker and the maximum temperature becomes higher. This suggests that multiple convection cells started to form at the upper part of the USL but with opposite movements; thus, they will impede the rise of warm flow and start to form another convection layer. In this case, the original convection area is compressed and the heat flow is accumulated, which reduces the heat transfer efficiency.

Furthermore, we compare the steady solutions and turbulent snapshots for $\delta = 0.3$ and $Ra = 10^6$. The steady solution shown in figure 11(*a*) presented that plumes gradually

https://doi.org/10.1017/jfm.2025.396 Published online by Cambridge University Press

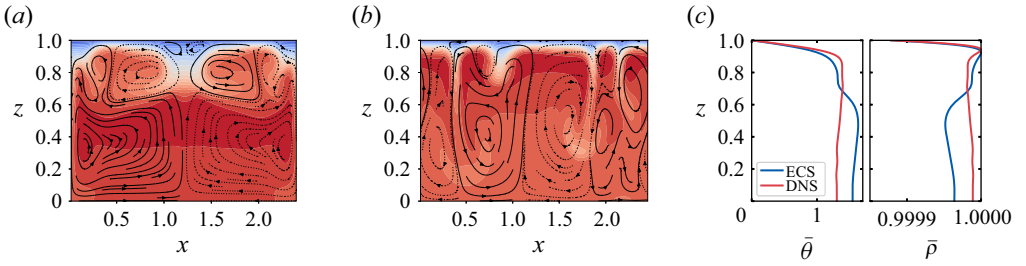


Figure 11. The flow field and temperature field for (a) exact coherent solution and (b) DNS result for $Ra = 10^6$ at $\delta = 0.3$ with other parameters $M = 18.125$ and $Pr = 10$. (c) The mean temperature $\bar{\theta}$ and density $\bar{\rho}$ profiles. The blue line is the exact coherent solution (ECS) and the red line is the DNS result.

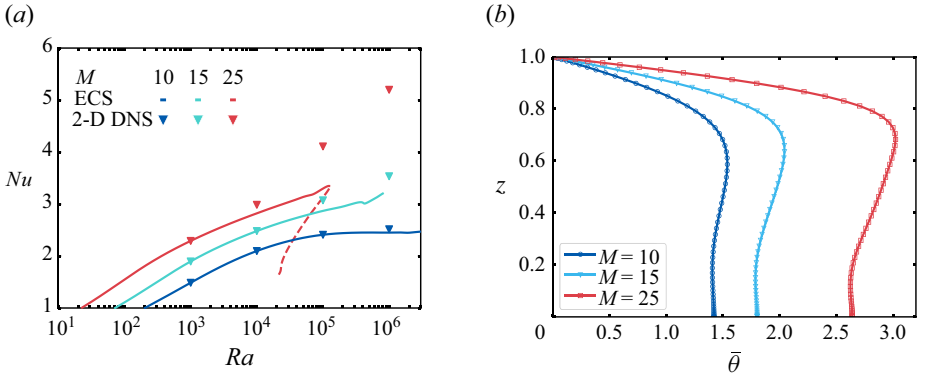


Figure 12. (a) The bifurcation diagram in the Ra–Nu plane with different values of M at $\delta = 0.6$ and $Pr = 10$ (ECS, exact coherent solution). (b) The horizontal mean temperature $\bar{\theta}$ for various values of M at $Ra = 10^4$ and $\delta = 0.6$.

formed a convection mixing layer at the upper layer of the USL. In this case, the fluid has divided into two convection layers with a decreasing staircase temperature profile with respect to heights (as shown in figure 11c). There is a higher temperature in the bottom and the staircase structure can be usually observed in later winter ice-covered lakes (Jansen *et al.* 2021). However, the unsteady results gained from DNS presented in figure 11(b) showed that the convection is more vigorous and unsteady, and the temperature profile is almost isothermal within the interior. These results suggest that the upper convection layer produced by secondary stratification hinders the effective mixing of heat in the system.

Figure 12(a) illustrates the bifurcation diagram at the same attenuation depth $\delta = 0.6$ with different dimensionless incoming heat flux M. It is obvious that higher M provides higher energy to the USL, and it is easier for the system to lose stability with a smaller critical value Ra_c. For various values of M, mean temperature profiles at $Ra = 10^4$ are plotted in figure 12(b). The profiles reveal that at a fixed attenuation depth δ, the position of maximum temperature is about the same and a higher incoming heat flux leads to a thinner SSL. Due to the larger thickness of the USL (d_{USL}) and the higher temperature difference (ΔT_{USL}), the characteristic Rayleigh number that is defined in terms of the USL

$$Ra^* = \frac{\alpha g \Delta T_{USL}^3 d_{USL}^3}{\nu\kappa} \tag{5.1}$$

https://doi.org/10.1017/jfm.2025.396 Published online by Cambridge University Press

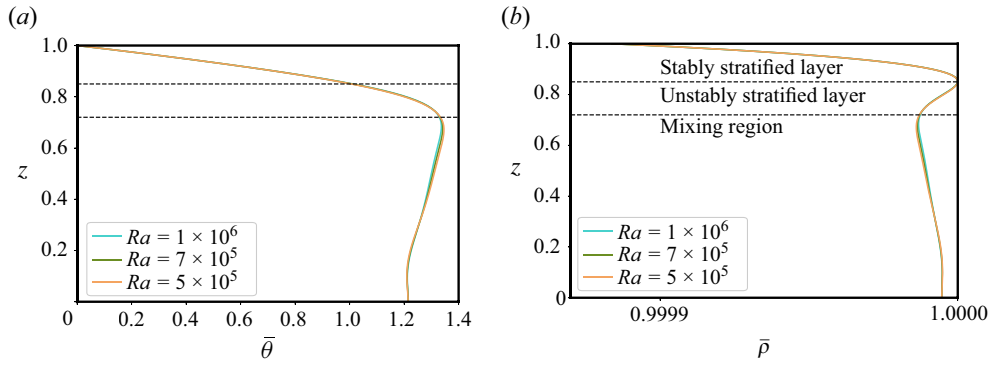


Figure 13. (*a*) The mean temperature $\bar{\theta}$ and (*b*) density $\bar{\rho}$ profiles. The horizontal dashed lines are the dividing lines of each layer. The other parameters are $\delta = 0.6$ and $M = 10$.

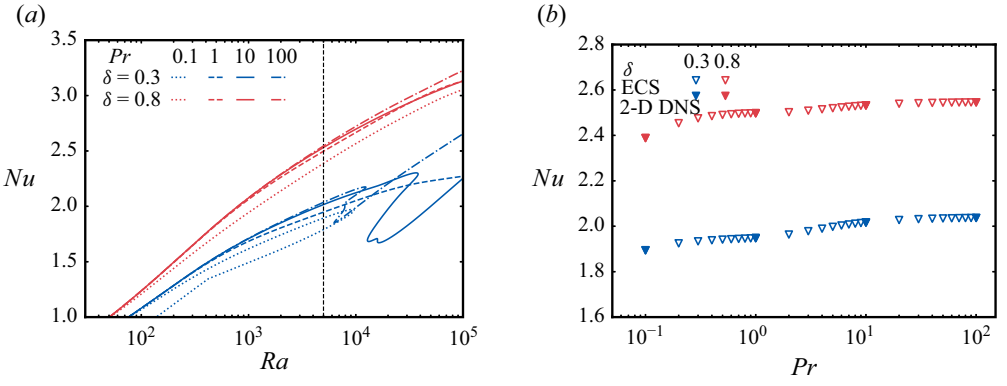


Figure 14. (*a*) The influence of Pr is shown on the bifurcation diagram in the Ra–Nu plane. The blue lines are for $\delta = 0.3$ and the red lines are for $\delta = 0.8$. (*b*) The Nusselt number Nu versus the Prandtl number Pr at $Ra = 5000$ (the vertical dashed line in *a*) with exact steady solutions (ECS) and DNS solutions. Blue patterns are for $\delta = 0.3$ and red ones are for $\delta = 0.8$.

becomes larger, and the system becomes more efficient in transporting heat. An interesting observation is that Nu becomes invariant for $M = 10$ even though Ra is raised. We plotted the mean temperature and density profiles (figure 13). We observed that the thickness of the USL and the temperature at the bottom layer do not change with increasing Ra (as shown in figure 13). Thus, the Nusselt number is basically the same in the range of $Ra \in [2 \times 10^5, 10^6]$. In addition, we have explored the Nu scaling, $Nu \sim Ra^{\gamma}$, within the range of $Ra \in [10^4, 10^6]$ for $M = 25$, and obtained the exponent $\gamma \approx 0.12$ by data fitting. However, when M is small, the scaling law is unclear, and we may be able to get a clear scaling law when Ra is larger.

The influence of the Prandtl number is examined over three decades, $10^{-1} \leqslant Pr \leqslant 10^2$, and results are illustrated in figure 14. When Ra is small, the data in figure 14(*a*) clearly show that Nu increases as Pr increases. However, when Ra is large, it is more reasonable to compare the heat transport of optimal steady-state or turbulent flow (Ding & Wu 2021), and we leave this for future study. It is obvious that the behaviour of the system near Ra_c is always supercritical, which is aligned with the outcomes from weakly nonlinear analysis (as shown in figure 7). When Pr exceeds a certain threshold, the flow pattern in the whole field becomes similar; for example, saddle-node bifurcations also appear when $Pr = 100$,

https://doi.org/10.1017/jfm.2025.396 Published online by Cambridge University Press

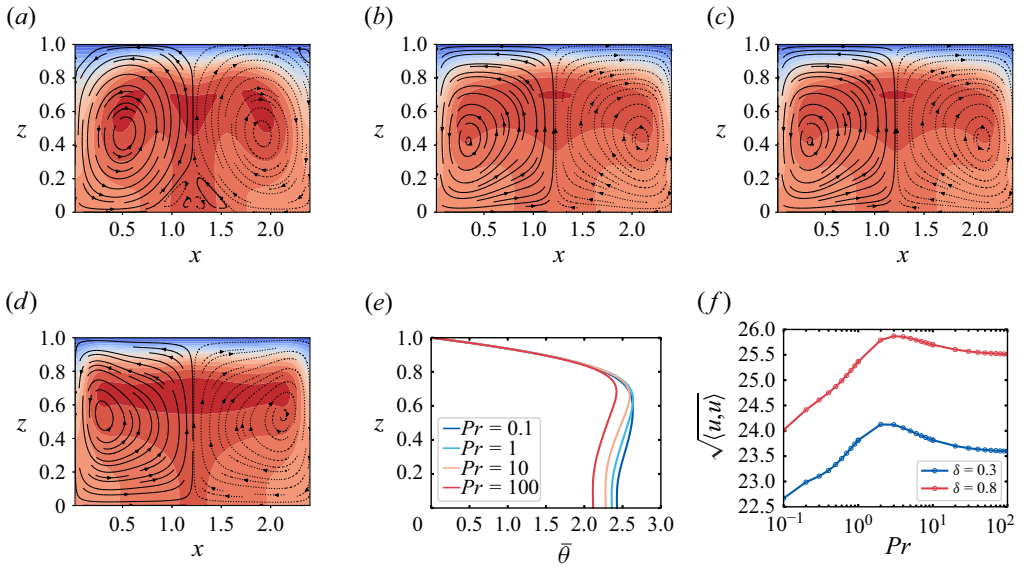


Figure 15. The flow field and temperature field from steady-state analysis at (*a*) $Pr = 0.1$, (*b*) $Pr = 1$, (*c*) $Pr = 10$ and (*d*) $Pr = 100$. The other parameters are $\delta = 0.3$, $Ra = 5000$. (*e*) The horizontal averaged temperature profile $\bar{\theta}$ for various values of Pr. (*f*) The root mean square of the velocity $\sqrt{\langle \boldsymbol{u}, \boldsymbol{u}\rangle}$ for different Pr with $\delta = 0.3$ and 0.8 and $Ra = 5000$.

which is similar to the case with $Pr = 10$ for $\delta = 0.3$. Figure 14(*b*) illustrates the influence of Pr on Nu for $Ra = 5000$. We observed that DNS results are aligned with exact coherent solutions and Nu slightly increases when $Pr < 10$, then becomes invariant when $Pr > 10$. Figure 15 displays the variations in fluid flow patterns and temperature fields with different Pr when $Ra = 5000$. It is obvious that the system has a cooler bottom temperature when the Prandtl number increases (as shown in figure 15*e*). When Pr becomes larger, $\sqrt{\langle \boldsymbol{u}, \boldsymbol{u}\rangle}$ increases, which makes the system strongly mixed and results in a higher Nu. However, beyond a threshold, the flow pattern seems not to change and $\sqrt{\langle \boldsymbol{u}, \boldsymbol{u}\rangle}$ decreases slightly (as shown in figure 15*f*). The value of Nu slightly increases then becomes insensitive to Pr, implying that a weaker flow can also transport more heat, which is somewhat counterintuitive.

6. Conclusion

This paper explored the linear and nonlinear dynamics of two-dimensional penetrative convection with radiative volumetric thermal forcing and a nonlinear density–temperature relationship. For this configuration, we considered that two plates are no-slip, and the temperature of the top plate is fixed and the bottom is adiabatic. The base state of the system is layered under the action of the forcing decay length and the incoming energy, which is divided into a SSL and an USL, and for smaller attenuation depths there also exists a NSL. Linear stability shows that with an increase of energy injection, the system becomes more unstable (as shown in Appendix A). We examined the effect of the dimensionless attenuation depth, δ, and incoming heat flux, M. We determined that the system has a minimal value of Ra_c around $\delta = 0.6$. For $\delta < 0.6$, Ra_c decreases as δ increases. As the thickness of the NSL becomes thinner, the unstable layer becomes thicker and the system is more susceptible to instability. If the attenuation lengths become

https://doi.org/10.1017/jfm.2025.396 Published online by Cambridge University Press

larger ($\delta > 0.6$), the magnitude of the internal heat term M/δ becomes smaller. Thus the temperature differences within the USL are smaller and the system becomes more stable again. At a given δ, we looked at the effect of incoming heat flux. More heat enters the system and makes a higher temperature difference within the USL. This results in a lower density and makes the system easily unstable.

We performed a weakly nonlinear analysis of the system to investigate the nonlinear effects. The findings revealed that the instability of the system is supercritical for all chosen δ and M. This is different from the penetrative convection studied by Veronis (1963) and Ding & Wu (2021), who proposed and determined that there exist non-trivial solutions in the subcritical instability region. The base-state temperature in our model causes the system to stratify into two layers: a SSL and an USL. When a finite-amplitude disturbance occurs, a homogeneous layer forms near the bottom and the USL becomes thinner, thus enhancing stability. This is unlike in the Veronis model, where a fixed bottom temperature leads to a thicker USL and instability at lower Rayleigh numbers. Near the critical bifurcation points, the results gained from the weakly nonlinear analysis are aligned with fully nonlinear bifurcation. In addition, we examined the impact of the Prandtl number Pr in the range of $0.1 \leqslant Pr \leqslant 100$. The results indicated that the magnitude of equilibrium amplitude $|A_{eq}|$ increases as Pr increases when $Pr < 10$, and it becomes almost the same when Pr is beyond a threshold. In particular, when Pr is large, the inertial effects become negligible and the effect of the Prandtl number diminishes.

Furthermore, the present work shows the bifurcation of the primary instability of the stationary base flow by seeking steady convection cell solutions and conducting DNS up to $Ra \sim O(10^6)$. It is clear that as Ra increases, the interior of the system is strongly mixed and the location of the maximal temperature shifts from the bottom to the inside. The unsteady motion gained from DNS showed a similar trend to that of the temperature profile but is closer to isothermal, which suggests a higher heat transport efficiency. An interesting observation is the existence of multiple steady solutions for a specific Ra. The flow pattern in the lower branch showed that smaller convection cells started to form in the upper part of the USL, and have an opposite flow direction. As Ra remains large, the fluid formed two convection layers with a staircase temperature profile, whereas this cannot be observed in the unsteady motion.

This paper also showed how the magnitude of incoming heat flux M affects the primary bifurcation. When M is small, there is an interesting result that the Nusselt number Nu stabilises at a constant value even though Ra is increasing. However, this does not happen at higher M; because of the large temperature difference, the system has enough energy to drive convection. In addition, the present work also demonstrated that the two-dimensional exact coherent solutions have a dependence on the Prandtl number Pr for both shallow and deep attenuation depths, $\delta = 0.3$ and $\delta = 0.8$. For $Pr < 10$, Nu increases slightly and becomes invariant when $Pr > 10$. As Pr increases, the flow speed increases, which makes the fluid strongly mixed and results in a higher heat transport efficiency. However, when Pr is beyond a threshold, the flow motion becomes slower, but Nu slightly increases and then becomes insensitive to Pr.

This paper gives an insight into the heat distribution in the water column beneath ice. In the current study, the numerical simulations have tracked up to $Ra \sim O(10^6)$ and found that the Nusselt number Nu depends on Pr, Ra, δ and M. However, when dealing with large-scale systems where Ra tends towards infinity, it is necessary to conduct further investigations to understand how the Nusselt number behaves under such extreme conditions and whether there exists a scaling law to predict the large-scale convection. Therefore, further simulations and analysis are needed to enhance our understanding of the underlying physical mechanisms involved.

https://doi.org/10.1017/jfm.2025.396 Published online by Cambridge University Press

Acknowledgements. The authors are supported by NSFC (no. 52176065). The authors extend their gratitude to the reviewers for their constructive feedback and insightful suggestions. We also thank the editors for their diligent handling of this paper and for facilitating a smooth review process.

Declaration of interests. The authors report no conflict of interest.

Appendix A. Contour plot with constant energy input

We took a transect through the plane presented in figure 3(*b*). The contour lines in figure 16 are the constant total input energy, and the colour in the background shows the critical Rayleigh number. As the attenuation depth δ increases, a larger incoming heat flux M is needed to balance the total energy input and make it a constant.

Appendix B. Weakly nonlinear analysis

Assume the weakly nonlinear solution is of the form (with its complex conjugate)

$$\psi(x, z, \tau) := \epsilon^{\alpha}\hat{\psi}_1(z)\mathrm{e}^{ikx}A(\tau) + \epsilon^{2\alpha}\left[\hat{\psi}_{20}(z) + \hat{\psi}_{22}(z)\mathrm{e}^{i2k}\right]A^2(\tau) + \cdots + \text{c.c.}, \quad \text{(B1)}$$

$$\tilde{\theta}(x, z, \tau) := \epsilon^{\alpha}\hat{\theta}_1(z)\mathrm{e}^{ikx}A(\tau) + \epsilon^{2\alpha}\left[\hat{\theta}_{20}(z) + \hat{\theta}_{22}(z)\mathrm{e}^{i2k}\right]A^2(\tau) + \cdots + \text{c.c.} \quad \text{(B2)}$$

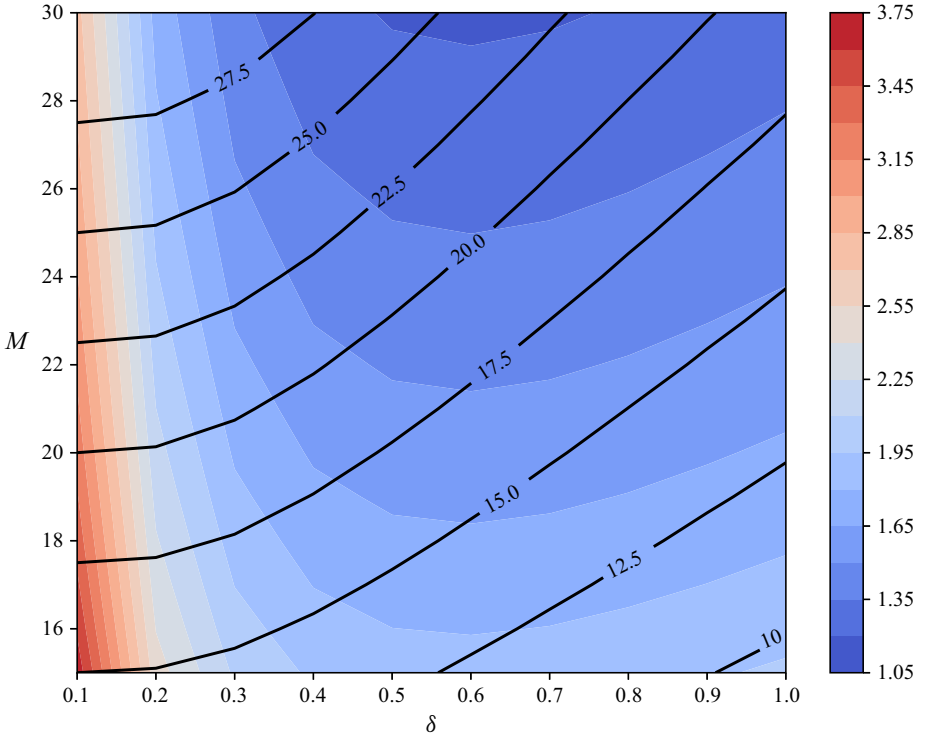


Figure 16. Contour plot with critical Rayleigh numbers. The contour lines represent the total energy input E. The colour in the background represents the critical Rayleigh number with $\log_{10} Ra$.

https://doi.org/10.1017/jfm.2025.396 Published online by Cambridge University Press

Substituting the assumptions (B1)–(B2) into equations (4.1)–(4.2) with $\omega = -\nabla^2\psi$ from the definition of vorticity and streamfunction and taking $\alpha = 1$, then we have

$$\left(\epsilon^3\frac{\partial\nabla^2\psi_1}{\partial\tau} + \epsilon^4\frac{\partial\nabla^2\psi_2}{\partial\tau} + \cdots\right) + \epsilon^2 J(\psi_1, \nabla^2\psi_1) + \epsilon^3 J(\psi_1, \nabla^2\psi_2) + \epsilon^3 J(\psi_2, \nabla^2\psi_1) + \cdots = 2\left(Ra_c + \epsilon^2 r\right) Pr\left(\theta_{st} - 1 + \left(\epsilon\tilde{\theta}_1 + \epsilon^2\tilde{\theta}_2 + \cdots\right)\right) \left(\epsilon\frac{\partial\tilde{\theta}_1}{\partial x} + \epsilon^2\frac{\partial\tilde{\theta}_2}{\partial x} + \cdots\right) + Pr\nabla^4\left(\epsilon\psi_1 + \epsilon^2\psi_2 + \cdots\right), \tag{B3}$$

and equation (4.2) becomes

$$\left(\epsilon^3\frac{\partial\tilde{\theta}_1}{\partial\tau} + \epsilon^4\frac{\partial\tilde{\theta}_2}{\partial\tau} + \cdots\right) + \epsilon^2 J(\psi_1, \tilde{\theta}_1) + \epsilon^3 J(\psi_1, \tilde{\theta}_2) + \epsilon^3 J(\psi_2, \tilde{\theta}_1) + \cdots = -\theta'_{st}\left(\epsilon\frac{\partial\psi_1}{\partial x} + \epsilon^2\frac{\partial\psi_2}{\partial x} + \cdots\right) + \nabla^2(\epsilon\tilde{\theta}_1 + \epsilon^2\tilde{\theta}_2 + \cdots), \tag{B4}$$

where $\psi_2 = [\hat{\psi}_{20}(z) + \hat{\psi}_{22}(z)\mathrm{e}^{i2k}]A^2(\tau) + \text{c.c.}$ and $\theta_2 = [\hat{\theta}_{20}(z) + \hat{\theta}_{22}(z)\mathrm{e}^{i2k}]A^2(\tau) + \text{c.c.}$

First we consider a linear problem in $O(\epsilon)$:

$$2Ra_c Pr(\theta_{st} - 1)\frac{\partial\tilde{\theta}_1}{\partial x} + Pr\nabla^4\psi_1 = 0, \tag{B5}$$

$$-\theta'_{st}\frac{\partial\psi_1}{\partial x} + \nabla^2\tilde{\theta}_1 = 0. \tag{B6}$$

It has a trivial solution with $\tilde{\theta}_1 = 0$ and $\psi_1 = 0$. However, we know that at $Ra = Ra_c$, there is a non-trivial solution since linear theory predicted that this is the point at which convection is just becoming linearly unstable. Taking $\boldsymbol{q}_i = [\psi_i, \tilde{\theta}_i]^T$, we then turn the above equations into a linear problem:

$$\mathcal{L}\boldsymbol{q}_1 = 0, \tag{B7}$$

where $\mathcal{L}$ is an operator given as

$$\mathcal{L} = \begin{pmatrix} Pr\nabla^4 & 2Ra_c Pr(\theta_{st} - 1)\dfrac{\partial}{\partial x} \\ -\theta'_{st}\dfrac{\partial}{\partial x} & \nabla^2 \end{pmatrix}. \tag{B8}$$

Recall the inner product of a complex function:

$$\langle\boldsymbol{q}_m, \boldsymbol{q}_n\rangle = \iint \psi^*_m\psi_n + \tilde{\theta}^*_m\tilde{\theta}_n \,\mathrm{d}z\mathrm{d}x. \tag{B9}$$

For the solvability conditions, the nonlinear term needs to be orthogonal to solutions of the adjoint homogeneous linear problem, which means that there exist $\boldsymbol{q}^\dagger$ spanning the kernel of $\mathcal{L}^\dagger$, i.e. $\mathcal{L}^\dagger\boldsymbol{q}^\dagger = 0$, and $\mathcal{L}^\dagger$ is the adjoint matrix of $\mathcal{L}$. Thus the solvability condition is satisfied:

$$\langle\boldsymbol{q}^\dagger_1, \mathcal{L}\boldsymbol{q}_m\rangle = \langle\mathcal{L}^\dagger\boldsymbol{q}^\dagger_1, \boldsymbol{q}_m\rangle = 0. \tag{B10}$$

https://doi.org/10.1017/jfm.2025.396 Published online by Cambridge University Press

Expressing the left-hand side by the definition of the inner product and applying integration by parts and the corresponding boundary conditions:

$$\begin{aligned}\langle \boldsymbol{q}_1^\dagger, \mathcal{L}\boldsymbol{q}_m\rangle &= \iint \psi_1^{\dagger *}\left(-Pr\nabla^4\psi_m + 2Ra_c Pr(1-\theta_{st})\frac{\partial\tilde{\theta}_m}{\partial x}\right)\\ &\quad + \tilde{\theta}_1^{\dagger *}\left(-\frac{\partial\theta_{st}}{\partial z}\frac{\partial\psi_m}{\partial x} + \nabla^2\tilde{\theta}_m\right)\mathrm{d}z\mathrm{d}x\\ &= \iint \psi_m\left(-Pr\nabla^4\psi_1^{\dagger *} + \frac{\partial\theta_{st}}{\partial z}\frac{\partial\tilde{\theta}_1^{\dagger *}}{\partial x}\right)\\ &\quad + \tilde{\theta}_m\left(-2Ra_c Pr(1-\theta_{st})\frac{\partial\psi_1^{\dagger *}}{\partial x} + \nabla^2\tilde{\theta}_1^{\dagger *}\right)\mathrm{d}z\mathrm{d}x\\ &= \langle \mathcal{L}^\dagger\boldsymbol{q}_1^\dagger, \boldsymbol{q}_m\rangle. \end{aligned} \tag{B11}$$

As we assume about $\boldsymbol{q}_1$, $\boldsymbol{q}_1^*$ is the complex conjugate, and $\boldsymbol{q}_1^\dagger$ is the solution when solving the adjoint homogeneous equation $\mathcal{L}^\dagger\boldsymbol{q}_1^\dagger = 0$. We also need to turn the boundary conditions into adjoint ones. This is also significant even though the boundary condition is the same as the original one in this case.

Next we think about the $O(\epsilon^2)$ term:

$$2Ra_c Pr(\theta_{st}-1)\frac{\partial\tilde{\theta}_2}{\partial x} + Pr\nabla^4\psi_2 = J(\psi_1, \nabla^2\psi_1) - 2Ra_c Pr\tilde{\theta}_1\frac{\partial\tilde{\theta}_1}{\partial x}, \tag{B12}$$

$$-\theta_{st}'\frac{\partial\psi_2}{\partial x} + \nabla^2\tilde{\theta}_2 = J(\psi_1, \tilde{\theta}_1). \tag{B13}$$

The left-hand side can be seen as $\mathcal{L}\boldsymbol{q}_2$, and the right-hand side is the nonlinear term. We substitute the assumptions into (B12)–(B13) and get the expansion for both right- and left-hand sides. Recall the no-slip velocity boundary conditions and temperature boundary conditions. We can use the above equations to determine the expression of $\hat{\psi}_{20}$, $\hat{\theta}_{20}$, $\hat{\psi}_{22}$ and $\hat{\theta}_{22}$.

Returning to $O(\epsilon^3)$, the set of equation now becomes

$$\begin{aligned}2Ra_c Pr(\theta_{st}-1)\frac{\partial\tilde{\theta}_3}{\partial x} + Pr\nabla^4\psi_3 &= \frac{\partial\nabla^2\psi_1}{\partial\tau} + J(\psi_1, \nabla^2\psi_2)\\ &\quad + J(\psi_2, \nabla^2\psi_1) - 2Ra_c Pr\left(\tilde{\theta}_1\frac{\partial\tilde{\theta}_2}{\partial x} + \tilde{\theta}_2\frac{\partial\tilde{\theta}_1}{\partial x}\right),\end{aligned} \tag{B14}$$

$$-\theta_{st}'\frac{\partial\psi_3}{\partial x} + \nabla^2\tilde{\theta}_3 = \frac{\partial\tilde{\theta}_1}{\partial\tau} + J(\psi_1, \tilde{\theta}_2) + J(\psi_2, \tilde{\theta}_1), \tag{B15}$$

where N_3 are the nonlinear terms in $O(\epsilon^3)$ as shown on the right-hand side, and then the set of equations can be considered as $\mathcal{L}\boldsymbol{q}_3 = N_3$, where $\boldsymbol{q}_3 = [\psi_3\ \tilde{\theta}_3]^T$. For the solvability condition, the nonlinear terms which have e^{ikx} need to be orthogonal to $\boldsymbol{q}_1^\dagger$, with the

https://doi.org/10.1017/jfm.2025.396 Published online by Cambridge University Press

complex inner product. Therefore, we will have

$$(\mathcal{A}_{11}+\mathcal{B}_{11})\frac{\mathrm{d}A}{\mathrm{d}\tau}+\mathcal{A}_{12}rA+(\mathcal{A}_{13}+\mathcal{B}_{13})|A|^2A=0, \tag{B16}$$

where

$$\mathcal{A}_{11}=-\int_0^1(D^2-k^2)\hat{\psi}_1\cdot\hat{\psi}_1^{\dagger *}\mathrm{d}z, \tag{B17}$$

$$\mathcal{A}_{12}=-\int_0^1 2\mathrm{i}kPr(\theta_{st}-1)\hat{\theta}_1\cdot\hat{\psi}_1^{\dagger *}\mathrm{d}z, \tag{B18}$$

$$\mathcal{A}_{13}=\int_0^1 N_{13}\cdot\hat{\psi}_1^{\dagger *}\mathrm{d}z, \tag{B19}$$

and

$$\mathcal{B}_{11}=\int_0^1\hat{\theta}_1\cdot\hat{\theta}_1^{\dagger *}\mathrm{d}z, \tag{B20}$$

$$\mathcal{B}_{13}=\int_0^1 N_{23}\cdot\hat{\theta}_1^{\dagger *}\mathrm{d}z, \tag{B21}$$

where N_{13} and N_{23} are the nonlinear terms of N_3 with e^{ikx}, and are expressed with the assumptions of the first-order and second-order solutions. If we consider it in the form of a pitchfork bifurcation $(\mathrm{d}A/\mathrm{d}\tau)=\lambda_1 rA+\lambda_2|A|^2A$, then

$$\begin{aligned}\lambda_1&=-\frac{\mathcal{A}_{12}}{\mathcal{A}_{11}+\mathcal{B}_{11}}\\&=-\frac{-\int_0^1 2\mathrm{i}kPr(1-\theta_{st})\hat{\theta}_1\cdot\hat{\psi}_1^{\dagger *}\mathrm{d}z}{-\int_0^1(D^2-k^2)\hat{\psi}_1\cdot\hat{\psi}_1^{\dagger *}\mathrm{d}z+\int_0^1\hat{\theta}_1\cdot\hat{\theta}_1^{\dagger *}\mathrm{d}z},\end{aligned} \tag{B22}$$

$$\begin{aligned}\lambda_2&=-\frac{\mathcal{A}_{13}+\mathcal{B}_{13}}{\mathcal{A}_{11}+\mathcal{B}_{11}}\\&=-\frac{\int_0^1 N_{13}\cdot\hat{\psi}_1^{\dagger *}\mathrm{d}z+\int_0^1 N_{23}\cdot\hat{\theta}_1^{\dagger *}\mathrm{d}z}{-\int_0^1(D^2-k^2)\hat{\psi}_1\cdot\hat{\psi}_1^{\dagger *}\mathrm{d}z+\int_0^1\hat{\theta}_1\cdot\hat{\theta}_1^{\dagger *}\mathrm{d}z}.\end{aligned} \tag{B23}$$

The results of the weakly nonlinear analysis are validated by an independently developed branch continuation routine. The governing equations are then discretised in space using Fourier modes in x and Chebyshev modes in z across the domain $(x,z)\in[-\pi/k,\pi/k]\times[0,1]$. Simulations for the curves appearing in figure 4 were run at 31 Chebyshev and 60 Fourier modes, and resolution independence was carefully checked at the terminal point of each branch shown.

We compared the results by taking a root mean square of the velocity over the whole domain, which is normally defined as

$$\sqrt{\langle\boldsymbol{u},\boldsymbol{u}\rangle}=\sqrt{\frac{k}{4\pi}\int_0^1\int_{-\pi/k}^{\pi/k}u^2+w^2\mathrm{d}x\,\mathrm{d}z}. \tag{B24}$$

https://doi.org/10.1017/jfm.2025.396 Published online by Cambridge University Press

Appendix C. Newton method for steady solutions

We begin with the steady governing equations:

$$F_\psi = \nabla^2\psi + \omega = 0, \tag{C1}$$

$$F_\omega = J(\psi, \omega) - \sqrt{\frac{Pr}{Ra}}\nabla^2\omega + 2(\theta - 1)\frac{\partial\theta}{\partial x} = 0, \tag{C2}$$

$$F_\theta = -J(\psi, \theta) + \frac{1}{\sqrt{Pr\,Ra}}\nabla^2\theta + \frac{1}{\sqrt{Pr\,Ra}}S(z) = 0. \tag{C3}$$

We solve the above steady equations from the critical linear stability point. The initial guess is thus given by the superposition of the conduction state and the eigenmode. The amplitude of the eigenmode is given by our weakly nonlinear analysis. Let us denote the initial guess as $\boldsymbol{h}_0 = [\psi_0, \omega_0, \theta_0]$, then a better guess is given as follows:

$$\boldsymbol{h} = \begin{bmatrix}\psi\\ \omega\\ \theta\end{bmatrix} = \begin{bmatrix}\psi_0\\ \omega_0\\ \theta_0\end{bmatrix} + \begin{bmatrix}\Delta\psi\\ \Delta\omega\\ \Delta\theta\end{bmatrix}. \tag{C4}$$

We denote $\Delta\boldsymbol{h} = (\Delta\psi, \Delta\omega, \Delta\theta)$. Substituting $\boldsymbol{h}$ into the governing equation and linearising around $\boldsymbol{h}_0$ (i.e. the Newton–Kantorovich approach) gives the following equation of $(\Delta\psi, \Delta\omega, \Delta\theta)$:

$$\mathbf{J}_{\boldsymbol{h}}(\boldsymbol{h}_0, Ra_0)\begin{bmatrix}\Delta\psi\\ \Delta\omega\\ \Delta\theta\end{bmatrix} = -\begin{bmatrix}F_\psi\\ F_\omega\\ F_\theta\end{bmatrix} = -\boldsymbol{F}(\boldsymbol{h}_0, Ra_0). \tag{C5}$$

In equation (C5), $\mathbf{J}_{\boldsymbol{h}}(\boldsymbol{h}_0, Ra_0)$ is the Jacobian matrix evaluated at $(\boldsymbol{h}_0, Ra_0)$ and

$$\mathbf{J}_{\boldsymbol{h}} = \begin{bmatrix} \mathscr{L} & I & 0\\ \dfrac{\partial\omega}{\partial z}\mathscr{D}_x - \dfrac{\partial\omega}{\partial x}\mathscr{D}_z & \dfrac{\partial\psi}{\partial x}\mathscr{D}_z - \dfrac{\partial\psi}{\partial z}\mathscr{D}_x - \sqrt{\dfrac{Pr}{Ra}}\mathscr{L} & 2(1-\theta)\mathscr{D}_x - 2\dfrac{\partial\theta}{\partial x}\\ -\dfrac{\partial\theta}{\partial z}\mathscr{D}_x + \dfrac{\partial\theta}{\partial x}\mathscr{D}_z & 0 & -\dfrac{\partial\psi}{\partial x}\mathscr{D}_z + \dfrac{\partial\psi}{\partial z}\mathscr{D}_x + \dfrac{1}{\sqrt{Ra\,Pr}}\mathscr{L}\end{bmatrix}, \tag{C6}$$

where $\mathscr{D}_x$ is the Fourier spectral differential matrix, $\mathscr{D}_z$ is the Chebyshev differential matrix, $\mathscr{L} = \mathscr{D}_x{}^2 + \mathscr{D}_z{}^2$ is the Laplacian operator and I is the identity matrix (see spectral methods in MATLAB by Trefethen (2000)). By imposing the boundary conditions, the above equations can be solved by a LU decomposition method. The iteration is terminated when $\|\Delta\boldsymbol{h}\|/\|\boldsymbol{h}\| \leqslant 10^{-8}$.

The branch continuation method is implemented to track the bifurcation diagram. This ensures that the solution follows a specific branch, avoiding jumps between disconnected branches. We denote the solutions of equations as $\boldsymbol{h}_0$ and Ra_0. To determine the next solution $\boldsymbol{h}_1$ and Ra_1 of equations (C1)–(C3), we substitute equation (C5) with $\boldsymbol{h}_1$ and Ra_1. The distance between two results is given as

$$F_s(\boldsymbol{h}_1, Ra_1) = \|\boldsymbol{h}_1 - \boldsymbol{h}_0\|_2^2 + (Ra_1 - Ra_0)^2 - \Delta s. \tag{C7}$$

https://doi.org/10.1017/jfm.2025.396 Published online by Cambridge University Press

To calculate the solution with a new Ra_1, we also need to form a matrix $\mathbf{J}_{Ra}$:

$$\mathbf{J}_{Ra} = \begin{bmatrix} 0 \\ -\frac{1}{2}Ra^{3/2}Pr^{1/2}\nabla^2\omega \\ -\frac{1}{2}Ra^{3/2}Pr^{-1/2}(\nabla^2\theta + S) \end{bmatrix}. \tag{C8}$$

Thus we can gain the solution by solving the following linearised equation:

$$\begin{bmatrix} \mathbf{J}_{\boldsymbol{h}}(\boldsymbol{h}_1, Ra_1) & \mathbf{J}_{Ra}(\boldsymbol{h}_1, Ra_1) \\ 2(\boldsymbol{h}_1 - \boldsymbol{h}_0)^T & 2(Ra_1 - Ra_0) \end{bmatrix} \begin{bmatrix} \Delta\boldsymbol{h}_1 \\ \Delta Ra \end{bmatrix} = - \begin{bmatrix} \mathbf{F}(\boldsymbol{h}_1, Ra_1) \\ F_s(\boldsymbol{h}_1, Ra_1) \end{bmatrix}, \tag{C9}$$

in which $\mathbf{J}_{Ra}(\boldsymbol{h}_1, Ra_1)$ is evaluated at $(\boldsymbol{h}_1, Ra_1)$ and the last line corresponds to the linearised equation (C7).

References

Álvarez-Regueiro, Eva, V., Javier, P., Fernández-Seara, J., Fernández, J. & Lugo, L. 2019 Experimental convection heat transfer analysis of a nano-enhanced industrial coolant. *Nanomaterials* **9** (2), 267.

Barker, A.J., Dempsey, A.M. & Lithwick, Y. 2014 Theory and simulations of rotating convection. *Astrophys. J.* **791** (1), 13.

Barnes, D.F. & Hobbie, J.E. 1960 Rate of melting at the bottom of floating ice. Geological survey research: short papers in the geological sciences. *Geol. Surv. Prof. Paper* **400**, B392–B394.

Bengtsson, L. 1996 Mixing in ice-covered lakes. In *The First International Lake Ladoga Symposium* (eds. Heikki H. S., Viljanen M., Slepukhina T. & Murthy R.), pp. 91–97, Springer Netherlands.

Bergé, P. & Dubois, M. 1984 Rayleigh-Bénard convection. *Contemp. Phys.* **25** (6), 535–582.

Bodenschatz, E., Pesch, W. & Ahlers, G. 2000 Recent developments in Rayleigh-Bénard convection. *Annu. Rev. Fluid Mech.* **32** (1), 709–778.

Bouffard, D. *et al.* 2019 Under-ice convection dynamics in a boreal lake. *Inland Waters* **9** (2), 142–161.

Bouillaut, V., Lepot, S., Aumaître, S. & Gallet, B. 2019 Transition to the ultimate regime in a radiatively driven convection experiment. *J. Fluid Mech.* **861**, R5.

Chandrasekhar, S. 1961 *Hydrodynamic and Hydromagnetic Stability*. Oxford University Press.

Chang, Y. & Scotti, A. 2023 Characteristic scales during the onset of radiatively driven convection: linear analysis and simulations. *J. Fluid Mech.* **973**, A14.

Chen, C.-T.A. & Millero, F.J. 1986 Thermodynamic properties for natural waters covering only the limnological range 1. *Limnol. Oceanogr.* **31** (3), 657–662.

Christopher, T.W., Le Bars, M. & Smith, S.S.G.L. 2023 Linear and nonlinear stability of Rayleigh–Bénard convection with zero-mean modulated heat flux. *J. Fluid Mech.* **961**, A1.

Cortés, A. & Macintyre, S. 2020 Mixing processes in small arctic lakes during spring. *Limnol. Oceanogr.* **65** (2), 260–288.

Creyssels, M. 2020 Model for classical and ultimate regimes of radiatively driven turbulent convection. *J. Fluid Mech.* **900**, A39.

Cross, M.C. & Hohenberg, P.C. 1993 Pattern formation outside of equilibrium. *Rev. Mod. Phys.* **65** (3), 851–1112.

Davaille, A. & Jaupart, C. 1994 Onset of thermal convection in fluids with temperature-dependent viscosity: application to the oceanic mantle. *J. Geophys. Res.: Solid Earth* **99** (B10), 19853–19866.

Ding, Z., Huang, R. & Ouyang, Z. 2024 Scaling laws behind penetrative turbulence: history and perspectives. *Adv. Atmos. Sci.* **41**, 1881–1900.

Ding, Z. & Ouyang, Z. 2023 Penetrative convection: heat transport with marginal stability assumption. *J. Fluid Mech.* **960**, A26.

Ding, Z. & Wu, J. 2021 Coherent heat transport in two-dimensional penetrative Rayleigh-Bénard convection. *J. Fluid Mech.* **920**, A48.

Efremova, T.V. & Pal'shin, N.I. 2011 Ice phenomena terms on the water bodies of northwestern russia. *Russian Meteorol. Hydrol* **36** (8), 559–565.

Farmer, D.M. 1975 Penetrative convection in the absence of mean shear. *Q. J. R. Meteorol. Soc.* **101** (430), 869–891.

https://doi.org/10.1017/jfm.2025.396 Published online by Cambridge University Press

GEBHART, B. & MOLLENDORF, J.C. 1977 A new density relation for pure and saline water. *Deep Sea Res.* **24** (9), 831–848.
GOLUSKIN, D. 2016 *Internally Heated Convection and Rayleigh-Bénard Convection*. Springer.
GOLUSKIN, D. & VAN DER POEL, E.P. 2016 Penetrative internally heated convection in two and three dimensions. *J. Fluid Mech.* **791**, R6.
GOLUSKIN, D. & SPIEGEL, E.A. 2012 Convection driven by internal heating. *Phys. Lett. A* **377** (1-2), 83–92.
GOTZINGER, G. 1909 Studien über das eis des lunzer unter-und obersees. *Internationale Revue der Gesamten Hydrobiologie Und Hydrographie* **2** (3), 386–396.
GRACE, A.P., FOGAL, A. & STASTNA, M. 2023 Restratification in late winter lakes induced by cabbeling. *Geophys. Res. Lett.* **50** (14), e2023GL103402.
GRACE, A.P., STASTNA, M., LAMB, K. & SCOTT, K. ANDREA 2022 Numerical simulations of the three-dimensionalization of a shear flow in radiatively forced cold water below the density maximum. *Phys. Rev. Fluids* **7** (2), 023501.
GROSSMANN, S. & LOHSE, D. 2004 Fluctuations in turbulent Rayleigh–Bénard convection: the role of plumes. *Phys. Fluids* **16** (12), 4462–4472.
HAMPTON, S.E. *et al.* 2017 Ecology under lake ice. *Ecol. Lett.* **20** (1), 98–111.
HUSSEIN, A.M., BAKAR, R.A. & KADIRGAMA, K. 2014 Study of forced convection nanofluid heat transfer in the automotive cooling system. *Case Stud. Therm. Engng* **2**, 50–61.
JANSEN, J. *et al.* 2021 Winter limnology: how do hydrodynamics and biogeochemistry shape ecosystems under ice? *J. Geophys. Res.: Biogeosci.* **126** (6), e2020JG006237.
JOSEPH, D.D. 1976 *Stability of Fluid Motions II*. Springer.
KAZEMI, S., OSTILLA-MÓNICO, R. & GOLUSKIN, D. 2022 Transition between boundary-limited scaling and mixing-length scaling of turbulent transport in internally heated convection. *Phys. Rev. Lett.* **129** (2), 024501.
KIPPENHAHN, R. & WEIGERT, A. 1990 *Stellar Structure and Evolution*. Springer.
KIRILLIN, G. *et al.* 2012 Physics of seasonally ice-covered lakes: a review. *Aquat. Sci.* **74**, 659–682.
KIRILLIN, G. & TERZHEVIK, A. 2011 Thermal instability in freshwater lakes under ice: effect of salt gradients or solar radiation? *Cold Reg. Sci. Technol.* **65** (2), 184–190.
LECOANET, D., BARS, L., MICHAEL, B., KEATON, J., VASIL, G.M., BROWN, B.P., QUATAERT, E. & OISHI, J.S. 2015 Numerical simulations of internal wave generation by convection in water. *Phys. Rev. E* **91** (6), 063016.
LEPOT, S., AUMAÎTRE, S. & GALLET, B. 2018 Radiative heating achieves the ultimate regime of thermal convection. *Proc. Natl Acad. Sci. USA* **115** (36), 8937–8941.
LEPPÄRANTA, M., TERZHEVIK, A. & SHIRASAWA, K. 2010 Solar radiation and ice melting in lake vendyurskoe, Russian karelia. *Hydrol. Res.* **41** (1), 50–62.
MALKUS, W.V.R. 1960 Considerations on localized velocity fields in stellar atmospheres. In *Aerodynamic Phenomena in Stellar Atmospheres IAU Symposium 12* (ed. R.N. Thomas), Zanichelli, p. 346.
MATTHEWS, P.C. & HEANEY, S.I. 1987 Solar heating and its influence on mixing in ice-covered lakes. *Freshwater Biol.* **18** (1), 135–149.
MCCUTCHAN, A.L. & JOHNSON, B.A. 2022 Laboratory experiments on ice melting: a need for understanding dynamics at the ice-water interface. *J. Mar. Sci. Engng* **10** (8), 1008.
MCDOUGALL, T. J., JACKETT, D.R., WRIGHT, D.G. & FEISTEL, R. 2003 Accurate and computationally efficient algorithms for potential temperature and density of seawater. *J. Atmos. Ocean. Tech.* **20** (5), 730–741.
MIRONOV, D., TERZHEVIK, A., KIRILLIN, G., JONAS, T., MALM, J. & FARMER, D. 2002 Radiatively driven convection in ice-covered lakes: observations, scaling, and a mixed layer model. *J. Geophys. Res.: Oceans* **107** (C4), 7–1.
MOORE, D.R. & WEISS, N. 1973 Nonlinear penetrative convection. *J. Fluid Mech.* **61** (3), 553–581.
MUSMAN, S. 1968 Penetrative convection. *J. Fluid Mech.* **31** (2), 343–360.
OLSTHOORN, J., TEDFORD, E.W. & LAWRENCE, G.A. 2021 The cooling box problem: convection with a quadratic equation of state. *J. Fluid Mech.* **918**, A6.
PLUMLEY, M. & JULIEN, K. 2019 Scaling laws in rayleigh-bénard convection. *Earth Space Sci.* **6** (9), 1580–1592.
PONCE, G.H.S.F., ALVES, M., MIRANDA, J.C.C., MACIEL FILHO, R. & WOLF MACIEL, M.R. 2015 Using an internally heat-integrated distillation column for ethanol–water separation for fuel applications. *Chem. Engng Res. Des.* **95**, 55–63.
POWERS, S.M. & HAMPTON, S.E. 2016 Winter limnology as a new frontier. *Limnol. Oceanogr. Bull.* **25** (4), 103–108.

https://doi.org/10.1017/jfm.2025.396 Published online by Cambridge University Press

RAMÓN, C.L., ULLOA, H.N., DODA, T., WINTERS, K.B. & BOUFFARD, D. 2021 Bathymetry and latitude modify lake warming under ice. *Hydrol. Earth Syst. Sci.* **25** (4), 1813–1825.
RICARD, Y. 2007 Physics of mantle convection. *Treatise Geophys.* **7**, 31–87.
SCHMID, P.J. & HENNINGSON, D.S. 2002 *Stability and Transition in Shear Flows*. Springer.
SCHUBERT, G. 2015 *Treatise On Geophysics*. Elsevier.
SHEN, Y., ZIKANOV, O. 2016 Thermal convection in a liquid metal battery. *Theor. Comput. Fluid Dyn.* **30** (4), 275–294.
SMIRNOV, S., SMIRNOVSKY, A., ZDOROVENNOVA, G., ZDOROVENNOV, R., EFREMOVA, T., PALSHIN, N. & BOGDANOV, S. 2023 Numerical simulation of radiatively driven convection in a small ice-covered lake with a lateral pressure gradient. *Water* **15** (22), 3953.
SMIRNOV, S., SMIRNOVSKY, A., ZDOROVENNOVA, G., ZDOROVENNOV, R., PALSHIN, N., NOVIKOVA, I., TERZHEVIK, A. & BOGDANOV, S. 2022 Water temperature evolution driven by solar radiation in an ice-covered lake: a numerical study and observational data. *Water* **14** (24), 4078.
TOPPALADODDI, S. & WETTLAUFER, J.S. 2018 Penetrative convection at high Rayleigh numbers. *Phys. Rev. Fluids* **3** (4), 043501.
TREFETHEN, L. N. 2000 *Spectral methods in MATLAB*. SIAM.
ULLOA, H.N., WINTERS, K.B., WÜEST, A. & BOUFFARD, D. 2019 Differential heating drives downslope flows that accelerate mixed-layer warming in ice-covered waters. *Geophys. Res. Lett.* **46** (23), 13872–13882.
ULLOA, H.N., WÜEST, A. & BOUFFARD, D. 2018 Mechanical energy budget and mixing efficiency for a radiatively heated ice-covered waterbody. *J. Fluid Mech.* **852**, R1.
VERESCAGIN, G. 1925 A selection of works from lake baikal expedition. *Dokl. Akad. Nauk SSSR* **12**, 161–164.
VERONIS, G. 1963 Penetrative convection. *Astrophys. J.* **137**, 641–663.
WANG, Q., ZHOU, Q., WAN, Z.-H. & SUN, D.-J. 2019 Penetrative turbulent Rayleigh–Bénard convection in two and three dimensions. *J. Fluid Mech.* **870**, 718–734.
WANG, Z., CALZAVARINI, E., SUN, C. & TOSCHI, F. 2021 How the growth of ice depends on the fluid dynamics underneath. *Proc. Natl Acad. Sci.* **118** (10), e2012870118.
WINTERS, K.B., ULLOA, H.N., WÜEST, A. & BOUFFARD, D. 2019 Energetics of radiatively heated ice-covered lakes. *Geophys. Res. Lett.* **46** (15), 8913–8925.
YANG, B., WELLS, M.G., LI, J. & YOUNG, J. 2020 Mixing, stratification, and plankton under lake-ice during winter in a large lake: implications for spring dissolved oxygen levels. *Limnol. Oceanogr.* **65** (11), 2713–2729.
YANG, B., YOUNG, J., BROWN, L. & WELLS, M. 2017 High-frequency observations of temperature and dissolved oxygen reveal under-ice convection in a large lake. *Geophys. Res. Lett.* **44** (24), 12–218.
ZDOROVENNOVA, G. *et al.* 2021 Dissolved oxygen in a shallow ice-covered lake in winter: effect of changes in light, thermal and ice regimes, *Water* **13** (17), 2435.

https://doi.org/10.1017/jfm.2025.396 Published online by Cambridge University Press